International Journal of Rock Mechanics & Mining Sciences 140 (2021) 104585

Contents lists available at ScienceDirect

International Journal of Rock Mechanics and Mining Sciences

journal homepage: http://www.elsevier.com/locate/ijrmms

A fully automatic-image-based approach to quantifying the geological strength index of underground rock mass

Sen Yang [a], Shimin Liu [b,*], Nong Zhang [c], Guichen Li [c,**], Jie Zhang [a]

[a] School of Energy Science and Engineering, Xi'an University of Science and Technology, Xi'an, 710054, PR China
[b] Department of Energy and Mineral Engineering, G3 Center and Energy Institute, The Pennsylvania State University, University Park, PA, 16802, USA
[c] Key Laboratory of Deep Coal Resource Mining, Ministry of Education of China; School of Mines; China University of Mining and Technology, Xuzhou, 221116, PR China

ARTICLE INFO

Keywords:
Digital image analysis
Geological strength index (GSI)
Fully automatic algorithms

ABSTRACT

The conventional discontinuity survey process in the mining industry is known to be a time-consuming one and it is technically challenging due to the limited accessibility of fresh rock exposures. A rapid and robust rock mass property quantification system is desirable for rock structure design during mining operations. In this work we develop an image-based and fully automatic rock mass Geological Strength Index (GSI) rating system. The proposed method involves a series of novel algorithms to quantify the GSI rating based on data recovered from digital images. The proposed GSI system includes both Structure Rating (SR) and Joint Condition Digital Imaging (JCDI) to represent the bulk rock and discontinuity surface conditions of the rock mass. Local histogram equalization and self-adaptive gamma correction were introduced into the pre-processing of the rock face images. Compared to conventional histogram equalization, local histogram equalization can effectively restrain the uneven distribution of brightness often present. Self-adaptive gamma correction based on the image properties automatically enlarges the difference between discontinuity areas and intact rock. A novel algorithm combining region growing and the Hough transform is proposed for the automatic extraction of discontinuity areas. Laboratory and field tests demonstrated that the algorithm possesses an advantage over existing methods with regard to better noise suppression and that it can yield reasonable results for images taken in poor photography conditions. Discontinuities were characterized using a novel algorithm comprising area thinning, skeleton linking, spurs removal, and sampling. Using this algorithm, four parameters of the discontinuity can be quantified: length, orientation, separation width, and JRC value. The proposed approach was validated by two field-based case studies.

1. Introduction

Ground failure is one of the major geohazards affecting various underground operations, including mining roadway excavation, underground tunneling and construction, and many others. Ground-failure associated fatal incidents and expensive interruptions frequently occur all over the world[1–6] and are therefore a persistent concern for rock engineering practitioners.

The prerequisite for an optimal ground support design is an appropriate estimate of the engineering properties of the rock mass surrounding the underground excavations. Several rock mass classification methods are commonly used to derive quantitative information about rock mass engineering properties. Table 1 lists the input parameters considered in the four widely accepted rock mass classification systems including: rock mass rating (RMR),[7] tunneling quality index (Q-system),[8] geological strength index (GSI),[9,10] and coal mine roof rating (CMRR).[11] The percentage ratio of discontinuity-based points to overall points for each system has been added to the bottom of Table 1. It can be seen that an overriding importance has been given to the discontinuity-based parameters (Due to the multiplication relationship of the Q-system, its ratio is hard to determine, however, four of six parameters are discontinuity-based, which suggests a similarly weighted distribution to other systems); in the GSI system, discontinuity-based parameters account for 100%—demonstrating that an accurate

* Corresponding author.
** Corresponding author.
E-mail addresses: szl3@psu.edu (S. Liu), liguichen@cumt.edu.cn (G. Li).

https://doi.org/10.1016/j.ijrmms.2020.104585
Received 25 April 2020; Received in revised form 26 November 2020; Accepted 21 December 2020
Available online 2 March 2021
1365-1609/© 2021 Elsevier Ltd. All rights reserved.

estimation of discontinuity is essential for rock mass classifications.

The conventional discontinuity field survey requires the operator to perform contact measurements on a rock exposure (natural outcrops, rock cuts or tunnel walls) using three methods: (a) scanline sampling; (b) circle sampling; and (c) area (or window) sampling.[13] The limitations of these methods are commonly recognized and can be summarized as the risks associated with proximity to unsupported rock exposures, the inaccessibility of sampling objects, the biases associated with visual observation, and the inefficiency resulting from labor-intensive and time-consuming field surveys. Emerging remote sensing techniques such as terrestrial laser scanning (also known as light detection and ranging [LiDAR]) and digital photogrammetry (including stereo photogrammetry [SP] and two-dimensional [2D] photogrammetry) show great potential for overcoming these limitations. By using practical techniques, rock engineers can remotely acquire a digitized representation of a rock exposure that records complete and accurate data on the discontinuity geometry in both a short period of time and a risk-free field environment. An increasing number of studies have been devoted to the automatic identification of discontinuities from the 3D point clouds captured from either LiDAR or SP.[14–19]

Nevertheless, the emergence of three shortcomings hinders further adoption of these techniques, especially in coal mine roadway driving. First, as pointed out by Zhang,[20] the current methods that includes principal curvature evaluation,[21–23] best-fit plane searching,[24–28] and local orientation clustering[29–35] can handle discontinuity recognition problems on a rock outcrop with discontinuity planes exposed (which is a common result from weathering erosion), but they exhibit low performance when dealing with embedded discontinuity planes (widely present on artificial rock cuts). Second, LiDAR and SP surveys involve several types of equipment (*e.g.* laser scanner, stereo camera, total station, and reference targets for point cloud alignment) and a complex arrangement.[33,36–38] Their implementation inevitably slows down the road driving speed and hinders the efficiency of ground support installation, which induces potential safety hazards. Third, the accuracy of a LiDAR survey is affected by the reflectivity of rock surfaces. The water-induced reduction of reflectivity will introduce a large number of blind spots in the data and therefore hamper further interpretations.[38] However, the water from either an underground aquifer or pump commonly appears in the working space of roadway driving and is a fact which cannot be avoided.[39,40] Roadway driving is confronting the variation of geomechanical properties in surrounding rock masses; therefore the excavation face is not only the sampling site, but also the object evaluated. Under such conditions, a flexible and adaptable technique is needed to provide operators with timely information on ground engineering properties.

In this study, we develop a system to automatically determine the GSI rating of a rock mass by analyzing its 2D digital images. The GSI is a user-friendly classification system in which the surface condition and interlocking of rock pieces are qualitatively considered.[41,42] The two parameters are estimated through visual observation of rock faces—and this unique feature enables the calculation of the GSI rating from image processing. Compared with LiDAR and SP, a 2D-photogrammetry survey is more suitable for discontinuity characterization in coal mine roadway driving because it has advantages in terms of a short survey process, flexible equipment arrangement, and high sensitivity to embedded discontinuity planes. We develop a quantified GSI system initially in Section 2. Then a fully-automatic algorithm for discontinuity recognition and characterization is proposed in Section 3. The algorithm is then applied to two field tests to evaluate its effectiveness and accuracy and validated through field work. The proposed technique can be used efficiently for rock mass property determination and provide the foundation for better ground control support design and implementation in the mines.

2. Background of GSI and proposed GSI quantification

The GSI system has a large number of advocates in the rock engineering field. However, it has an inherent flaw that the rating is derived from qualitative input parameters. Consequently, the process requires users to possess rich experience in geotechnical surveying and it is hard to avoid the influence of its excessive subjectivity. As previously stated, our work is an attempt to use image processing technology to achieve the automatic estimation of GSI input parameters, which inherently requires a quantification of the parameters with the consequence of making the estimated *GSI* more explicit. In this section, the Structure Rating (*SR*) by Sonmez and Ulusay[43,44] and a new parameter (*Joint Condition Digital Imaging Rating*) are introduced to provide a quantitative basis for evaluating the interlocking of rock pieces and the surface condition, respectively.

It can be observed in the GSI chart[41,42] that the rock mass structure is classified by estimating the degree of interlocking of rock pieces. This characteristic results in a scale-independent feature, *i.e.* the GSI system is insensitive to the variation in the volume of the rock pieces. Russo[45] used an example to illustrate the drawback of this feature. If there is a rock mass consisting of cubic rock blocks formed by three mutually orthogonal discontinuity sets, according to the GSI chart,[41,42] its structure should be identified as blocky. In this case, if the discontinuity system remains unchanged, a rock mass made up of cubic blocks of 1 cm^3 will be assigned the same rating as the one made up of blocks of 1 dm^3 (even 1 m^3). Consequently, a 5-m width roadway should exhibit the same engineering property in these two conditions. It is clear, based on practical experience, that this is far from the truth and also counter-intuitive. Knowing this limitation, researchers have used the fracturing degree as an alternative way to quantify the interlocking of rock pieces. Cai et al.[46] proposed a parameter—*Block Volume*—as a means for the quantification. This parameter can be considered as a volumetric expression of the discontinuity density. The quantitative estimation, as proposed, was to be based on the discontinuity spacing and the angle between discontinuity sets. However, for engineering projects conducted in sedimentary strata such as a coal seam, the

Table 1
Input parameters for rock mass classification systems (after Zhang[12] with CMRR added).

Classification System	RMR	Q-system	GSI	CMRR
Parameters	UCS	Discontinuity set number J_n	Surface condition	UCS
	RQD	RQD	Interlocking of rock blocks	Discontinuity persistence and spacing
	Discontinuity spacing	Discontinuity roughness J_r		Discontinuity shear strength
	Discontinuity condition	Discontinuity alternation J_a		Moisture Sensitivity Deduction:
	Ground water condition	Discontinuity water reduction factor J_w		
		Stress reduction factor *SRF*		
Adjustment Parameters	Discontinuity orientation			Multiple discontinuity Adjustment
Percentage of Discontinuity-based points	70 %	–	100 %	62–70 %

UCS denotes unconfined compressive strength of intact rock core, RQD denotes the rock quality designation.

recognition of discontinuity sets is extremely challenging. Agliardi et al.[47] suggested that, in borehole logging surveys, the discontinuity spacing can be used to characterize the interlocking degree of rock masses. This is an obviously biased measure of discontinuity geometry, and the reason for this is that discontinuity spacing is the only reliable information collected from the measurements of drill cores. Hoek et al.[48] presented a quantification of the interlocking based on a well-established parameter—*RQD*. In the case of a lack of borehole data, they recommended using an expression[49] to relate *RQD* to *volumetric joint count*, J_v.[50] The expression is shown in Equation (1):

$$RQD = 110 - 2.5J_v \quad (1)$$

Sonmez and Ulusay[43,44] defined *SR* as a logarithmic function of J_v:

$$SR = -17.5ln(J_v) + 79.8 \quad (2)$$

The range of J_v that corresponds to each structure type of the GSI system is calculated by using Equations (1) and (2). The results are listed in Table 2. The question that is then raised is which method is reliable and robust enough to give the most appropriate ranges for the structure types of the GSI. The ISRM (International Society for Rock Mechanics)[51] provided descriptive terms for several J_v ranges in order to visualize the different types of rock mass listed in Table 3. A one-to-one correspondence can be found between the terms given by ISRM and the structure types of GSI, and the J_v ranges derived by Equation (2) are well matched with ranges given by the ISRM. Obviously, *SR* is a robust and suitable method for the quantification of the interlocking of rock pieces.

Several scholars have offered assessment methods aimed at the quantification of surface conditions. Sonmez and Ulusay[43,44] proposed a new parameter (*Surface Condition Factor*) based on the RMR rating. Cai et al.[46] suggested simplifying the *Joint Condition Factor* of the Rock Mass index[52] as a quantified measure of the alteration of the joint surface. Russo[45] believed that the *Joint Condition Factor* of the Rock Mass index should be fully persevered in the quantification of surface condition. Hoek et al.[48] recommended that both the *Joint Condition Rating* (by RMR) and the quotient of *Joint Roughness Number* and *Joint Alteration Number* (by Q-system) are capable of quantifying the surface condition. Thus it is clear that scholars preferred to take the discontinuity condition parameter of mature rock mass classification systems as the benchmark quantification of surface condition. Therefore, we follow that convention and introduce a new parameter named the *Joint Condition Digital Imaging Rating* (*JCDI*). It is based on the *Separation Rating* (S_r) and *Roughness Rating* (R_r) of RMR (see Table 4) and can be expressed as:

$$JCDI = \frac{25}{6}(S_r + R_r) \quad (3)$$

The weight assigned for Equation (3) is to facilitate the further calculation of the GSI rating. The surface condition of the GSI system is collectively defined by roughness, weathering, and the joint filling of the rock mass as illustrated in the GSI chart.[41,42] Among them, the variation of roughness can be directly related to the value of R_r, while the weathering and filling are indirectly estimated by using S_r. It is hard to establish a uniform quantitative standard for the evaluation of the degree of weathering because the form of rocks shaped by weathering varies between different rock types and different weathering causes. However, it is certainly evident that weathering can definitely deteriorate a rock's strength through water-air-rock interactions. Therefore, when operators classify rock walls at a driving face, the excavation alteration of fracture separation can provide an indirect evaluation of the weathering degree. Moreover, the loss of filling during excavation is an indication of the compactness, and it can be captured by calculating the fracture separation on a digital photograph.

RMR only gives a qualitative definition for R_r. We suggest using the *Joint Roughness Coefficient* (*JRC*) as a tool to quantify it. Barton and Choubey[53] divided *JRC* into 10 ranges and added a description to each one of them (see Table 5). According to these descriptions, the sections of R_r are related to specific *JRC* values. But, a mathematical method is required to calculate *JRC* values from the profile geometry of discontinuities presented on digital photographs. Several surface parameters have been proposed to mathematically characterize the discontinuity roughness. Those that commonly measure the average deviation of profiles from a center line include the root mean square (*RMS*), center line average (*CLA*), *RMS* of the first derivative of the profile (Z_2), and *RMS* of the second derivative (Z_3). Those that characterize surface roughness by considering the distribution of asperity heights,[57] and thus are not affected by the change of center line, are mean square values (*MSV*), autocorrelation function (*ACF*), and structure function (*SF*).[54–57] This (SF) *JRC* characteristic can enhance the robustness of the image analysis algorithm. A regression analysis by Tse and Cruden[57] shows that *SF* has a much higher correlation with *JRC* (correlation coefficient = 0.984) than *MSV* and *ACF* (correlation coefficients are 0.690 and 0.688, respectively). Thus, the *SF* would be suitable for the characterization of discontinuity roughness on digital images. The relation between *JRC* and *SF* is expressed as follow[57]:

$$JRC = 2.69 + 245.70(SF) \quad (4)$$

The development of a quantified GSI system interfaced to digital image analysis is proposed here based on newly developed *Joint Condition Digital Imaging Rating* (*JCDI*) system. The newly proposed GSI chart is illustrated in Fig. 1. The rock mass structure and surface condition of the GSI chart are supplemented with *SR* and *JCDI* values. The total rating

Table 2
J_v (joints/m^3) ranges for the determination of structure types of the GSI.

Method	Intact or massive	Blocky	Very blocky	Blocky/ disturbed/ seamy	Disintegrated
Hoek et al.	<12.0	12.0–20.0	20.0–28.0	28.0–36.0	>36.0
Sonmez and Ulusay	<1.0	1.0–3.1	3.1–9.7	9.7–30.5	>30.5

Table 3
Descriptive terms for J_v ranges suggested by ISRM.[51]

Description terms	J_v (joints/m3)
Very large blocks	<1.0
Large blocks	1–3
Medium-sized blocks	3–10
Small blocks	10–30
Very small blocks	>30

Table 4
Definition of separation rating and roughness rating, after RMR.[7]

S_r	None	<0.1 mm	0.1–1.0 mm	1–5 mm	>5 mm
Rating	6	5	4	1	0
R_r	Very rough	Rough	Slightly rough	Smooth	Slickensided
Rating	6	5	3	1	0

Table 5
Descriptions of *JRC* ranges and corresponding sections of R_r.

JRC ranges	Descriptions by Barton and Choubey	R_r sections
20–18	Rough, irregular	Very rough
18–16	Rough, irregular	
16–14	Rough, undulating	Rough
14–12	Rough, undulating	
12–10	Rough, undulating	
10–8	Rough, planar	Slightly rough
8–6	Rough, planar	
6–4	Undulating, planar	Smooth
4–2	Smooth, planar	Slickensided
2–0	Smooth, planar	

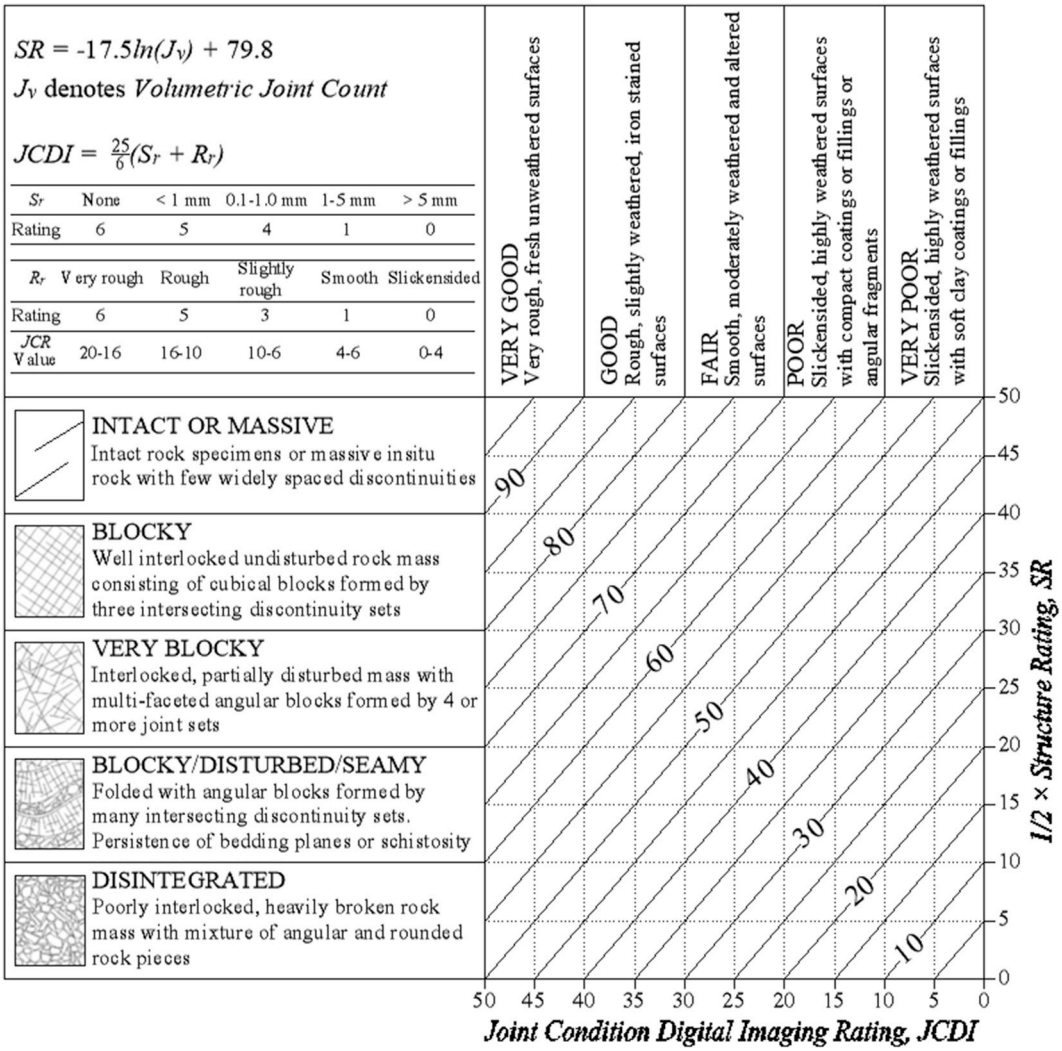

Fig. 1. Proposed quantified GSI system based on the *JCDI* rating.

of the *GSI* is obtained by using the following expression:

$$GSI = \frac{1}{2}SR + JCDI \tag{5}$$

3. Discontinuity characterization and quantification through image analyses

A fully-automatic algorithm for discontinuity recognition and characterization is detailed in this section. Full automation in order to eliminate manual intervention became an important consideration during the development process. The flow chart of the proposed method is presented in Fig. 2. First, the digital image of the exposed rock face is taken by using a high-resolution digital camera and the distance between lens and rock face is measured and recorded. Second, the rock face image is preprocessed by local histogram equalization and self-adaptive gamma correction. Third, region-growing segmentation and the Hough transform are utilized to extract discontinuous areas. Fourth, the discontinuity traces are separated from discontinuity areas by thinning, skeleton linking, and spur removal. Based on this result, the measurements of separation width and roughness are obtained. Finally, the GSI rating is derived by assigning values to the parameters in Equation (5). Details for each step are explained in the subsequent sections.

3.1. Digital image acquisition

3.1.1. Imaging device

The device for rock face imaging consists of a digital camera (GoPro CHDHX-601-RW) and a diffuse lamp. Fig. 3 shows the imaging devices working in a laboratory. A black backdrop is used to eliminate the interference of background because the laboratory-scale rock sample is not large enough to occupy the whole image. The GoPro camera has high-level performance and is waterproof, dustproof, and impact resistant—beneficial for imaging in a harsh underground environment. The specifications of the camera are given in Table 6. The diffuse lamp is employed because the diffuse lighting can eliminate shadows and glare and so enhance the accuracy and efficiency of noise filtering and discontinuity segmentation.[58–60] The perspective error and lens distortion are minimized by placing the camera normal to the rock face being sampled.

3.1.2. Relationship between image dimensions and real dimensions

A mathematical relationship between the dimensions of the discontinuity image and the real size of the rock mass is required for GSI classification. The geometrical relationship between field angle and focal length paves a way to tackling this challenge. The field angle is commonly used to evaluate the field of view (L_f) of a lens. By using the similar triangle theory of imaging,[60] the field of view can be expressed as a function of working distance (D_w, mm):

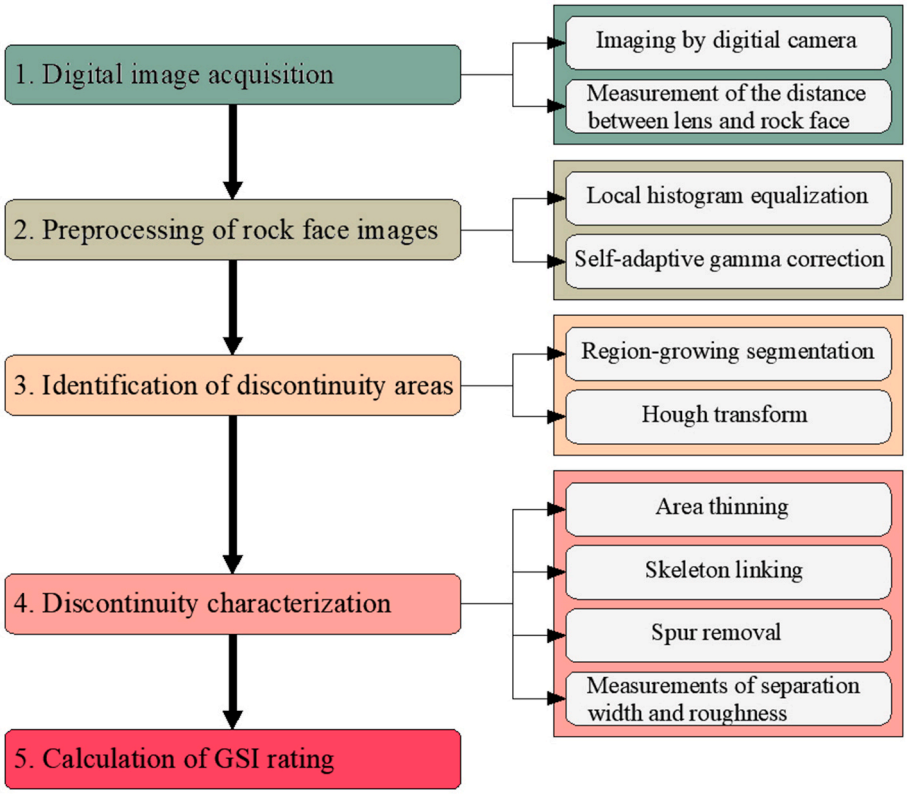

Fig. 2. Flow chart of the discontinuity recognition and characterization.

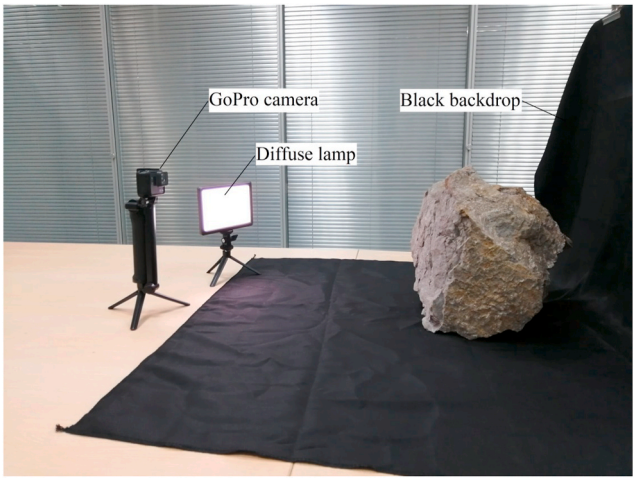

Fig. 3. The rock discontinuity imaging system in laboratory.

Table 6
Specifications of GoPro digital camera.

Sensor type	Size (mm)	Aspect ratio	Number of pixel (× 10^7)	Lens aperture	Digital zoom	Focal length (mm)
CMOS 1/2.3 inch	6.17 × 4.63	4:3	1.2	f/2.8	2 ×	4.3

$$L_f = (S_s \times D_w) \,/\, F \tag{6}$$

where S_s and F denote the sensor size (mm) and focal length (mm), respectively and these are listed in Table 6. The working distance is derived by measuring the distance between lens and rock face. Based on Equation (6), the height (H_f, mm) and width (W_f, mm) of the visible area are related to the height (H_p, in terms of pixel distance) and width (W_p, in terms of pixel distance) of an image by the following equations:

$$H_f = \left(H_p \times P_s \times D_w\right) \,/\, F \tag{7}$$

$$W_f = \left(W_p \times P_s \times D_w\right) \,/\, F \tag{8}$$

where P_s is the distance on the camera sensor represented by a unit pixel distance. According to the camera specifications in Table 6, it can be determined to be 1.543×10^{-3} mm.

An example of a discontinuity is shown in Fig. 4. The length (mm) and separation width (mm) are denoted by l_d and u_d, respectively. The length (in terms of pixel distance) and separation width (in terms of pixel distance) of its image are denoted by l_i and u_i, respectively. Based on Equations (7) and (8), the following equations can be derived.

$$l_d = (l_i \times P_s \times D_w) \,/\, F \tag{9}$$

$$u_d = (u_i \times P_s \times D_w) \,/\, F \tag{10}$$

Equations (9) and (10) enable us to derive length and separation width data from discontinuity images, which is fundamental to not only the calculation of *JCDI* but also the accuracy evaluation of the algorithm proposed in Section 3.4.

3.2. Preprocessing of rock face images for rock discontinuity quantification

Human eyes search for discontinuities on a digital image by

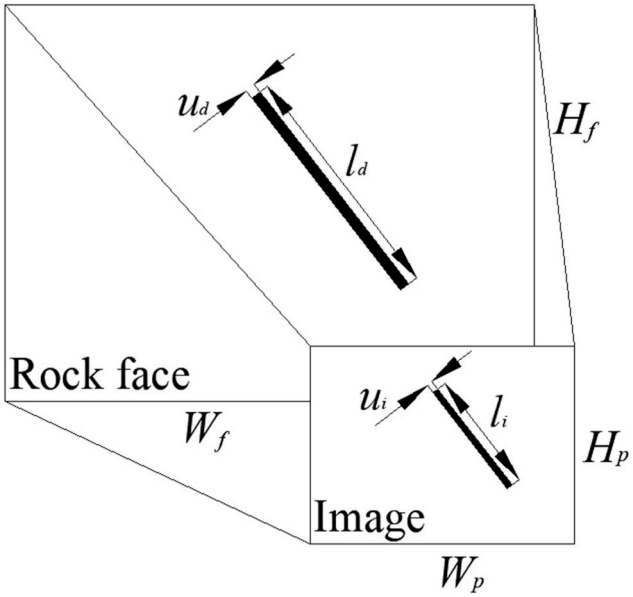

Fig. 4. Illustration of image dimensions and real dimensions for rock discontinuity.

observing the sharp variation in pixel intensity. If we liken the image to a surface with pixel intensity equating to elevation, then a "ravine" is found to be present at the fracture area.[61] The recognition of discontinuities is achieved by capturing the ravine structure; however, a noisy signal around the actual fracture can influence the direct application of this method, which may potentially give false fractures. Thus preprocessing is required to curb the noise and so increase the proportion of the desired signal in the digital images.

3.2.1. Description of image

In this work, an image of a fractured rock face was acquired at an imaging distance of 31.7 cm. The height and width of the rock face were ~25 cm by ~20 cm. This was then converted from the RGB format to a greyscale format by using Equation (11).

$$I = 0.299 \times R + 0.587 \times G + 0.114 \times B \tag{11}$$

where I is the light intensity of pixels, and R, G, and B denote the red, green, and blue components. The result (with a resolution of 1268 × 1671 pixels) is shown in Fig. 5a, and its histogram, which is supplemented as a statistic of pixel distribution, is calculated and shown in Fig. 5b.

3.2.2. Local histogram equalization

In Fig. 5b, it can be seen that pixels concentrate around a relatively high intensity level, *i.e.* 175. As a result, Fig. 5a appears to have a visual effect similar to overexposure. The concentration of pixels blurs the boundary between the intact rock face and discontinuities, thereby hindering the subsequent segmentation process. It is known that the histogram of an ideal ravine structure is characterized by a 'two-peak' distribution. The pixels constituting discontinuities and intact rock face gather around the two peaks. As a result, the segmentation process is easily accomplished by applying a thresholding algorithm.[62]

In order to facilitate the segmentation of the discontinuity shown in Fig. 5a, a local histogram equalization was used as a preliminary preprocessing procedure to enhance the contrast. The increase of contrast enlarges the gap between the highest and lowest intensity levels which helps to separate the low-level pixels constituting discontinuity areas from high-level pixels. Local histogram equalization was developed based on the conventional histogram equalization.[62] This method divides the virgin image into several regions and then applies histogram equalization for each. Subsequently, bilinear interpolation is used to eliminate boundary effects. The intensity levels in a greyscale image can be considered as random variables in the interval [0, 255]. Let r denotes the intensity of each pixel for the virgin image. The transformation function of conventional histogram equalization has the form:

$$TF(r) = 255 \sum_{i=0}^{r} (n_i \ / \ M) \tag{12}$$

where n_r is the number of pixels that have intensity level r. M denotes the sum of all pixels in the image.

We want to point out that the transformation function of conventional histogram equalization is commonly applied to the whole image. This process easily ignores localized rock structure features, which can lead to an uneven distribution of brightness. It can potentially result in false recognition of rock discontinuity in both bright and dark areas. The local histogram equalization can restrain the unevenness using the aforementioned division and processing. However, an excessive amount of division can induce the adverse effect of blurriness. To allow a comparison, Table 7 shows the changes caused by increasing the number of regions. The divided regions were defined by using different quantities of rows and columns as described in the parenthesis. It is apparent that the discontinuity traces tend to be blurred with an increase in the amount of noise. Based on this trial-and-error visual evaluation, a range

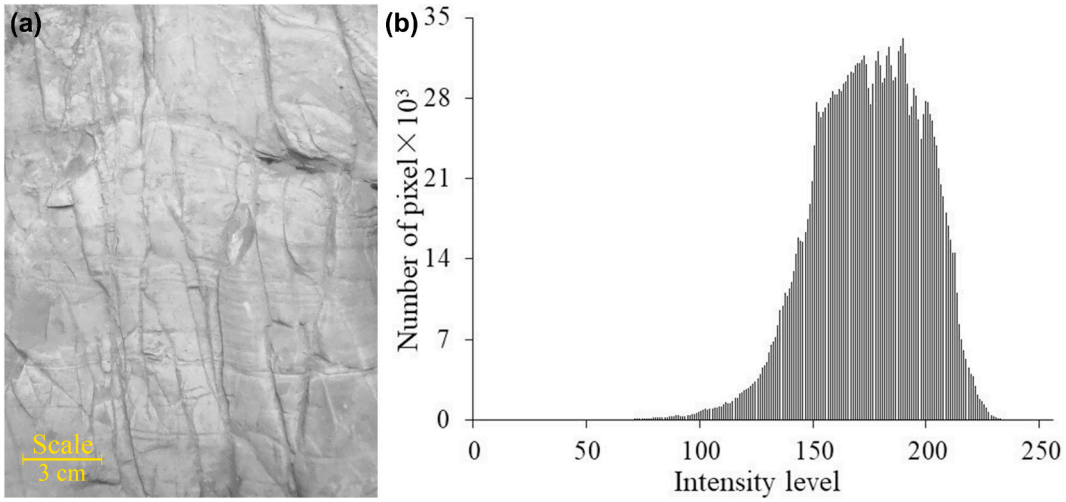

Fig. 5. (**a**) Greyscale image of a fractured rock face and (**b**) corresponding histogram.

Table 7
Number of regions and corresponding outcomes.

4 (2 × 2)	144 (12 × 12)	400 (20 × 20)	900 (30 × 30)	1600 (40 × 40)
				

of regions from 64 (8 × 8) to 256 (16 × 16) was recommended. In the current study we chose a total of 144 regions with 12 rows and 12 columns and the outcome is shown in Table 7. A visual assessment of the outcome indicates that the processed image brought out many more of the details of the discontinuities while at the same time the unevenness in brightness was effectively restrained.

3.2.3. Self-adaptive gamma correction

It can be seen from the outcome in Table 7 that the image appears dark and quite a few of the intact rock face pixels are at relatively low intensity levels. These intact rock low-intensity pixels could potentially be recognized as a discontinuity because of their similarity in pixel intensity to actual discontinuities. These image misrecognitions will reduce the accuracy of the segmentation process. Thus, a self-adaptive gamma correction was introduced to improve the contrast, which is expected to enlarge the difference between discontinuity areas and the intact rock face leading to ultimately eliminating the misrecognitions.

Self-adaptive gamma correction is developed by supplementing gamma correction with adaptivity. The transform function for gamma correction can be expressed as:

$$TG(r) = r_{max}(r/r_{max})^{\gamma} \tag{13}$$

where r denotes the intensity of each pixel for the input image, r_{max} is the maximum intensity of the image which is a constant of 255, and γ is a varying parameter used for histogram modification. It is essential to have an algorithm to automatically determine the value of γ based on properties of the various input images. Huang et al.[63] proposed a method to solve this problem by using the cumulative distribution function (cdf) and weighting distribution function (pdf_w). The method can be formulated as:

$$\gamma = 1 - cdf_w(r) \tag{14}$$

where,

$$cdf_w(r) = \sum_0^r pdf_w(j) \Big/ \sum pdf_w \tag{15}$$

$$\sum pdf_w = \sum_0^{r_{max}} pdf_w(j) \tag{16}$$

$$pdf_w(r) = pdf_{max}\left(\frac{pdf(r) - pdf_{min}}{pdf_{max} - pdf_{min}}\right)^{\beta} \tag{17}$$

$$pdf\ (r) = n_r/M \tag{18}$$

where r has the same definition as in Equation (13), β is an adjustable parameter, n_r denotes the number of pixels with intensity level r, M denotes the sum of pixels in the input image, pdf_{max} and pdf_{min} denote the maximum and minimum values of Equation (18), respectively. The outcomes of applying this procedure are presented in Fig. 6. The rock face in Fig. 6a is dramatically brightened, meanwhile the discontinuity areas are preserved. Comparing Fig. 6b with Fig. 5b, we can observe that a large portion of the pixels have been mapped to high levels, thus, the proportion of pixels constituting discontinuity areas to low-level pixels is increased, which is beneficial to the segmentation of discontinuities.

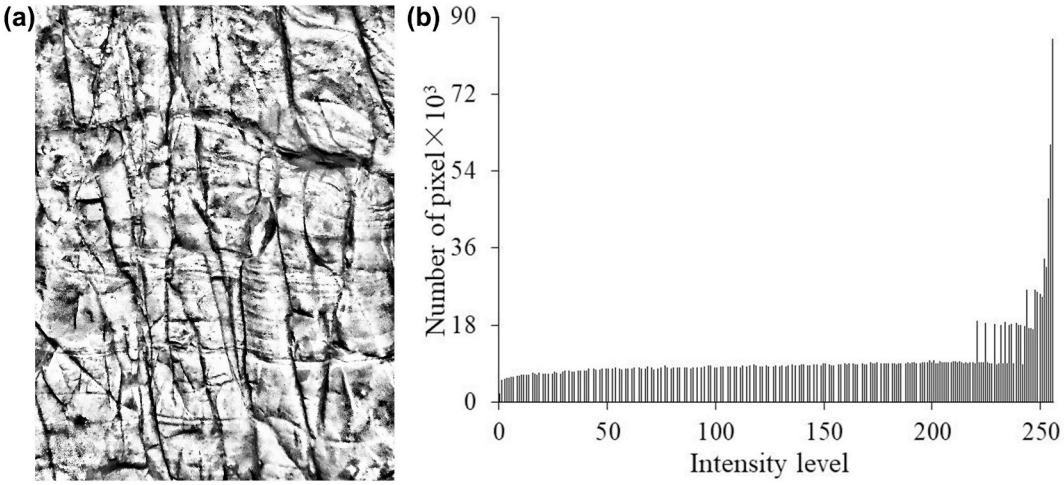

Fig. 6. (**a**) Outcome of self-adaptive gamma correction and (**b**) the corresponding histogram.

3.3. Identification of discontinuity areas

The ultimate goal of the image analysis is to obtain a robust, automated and reliable discontinuity quantification and this depends on having accurate discontinuity traces. Therefore, a high-performance segmentation algorithm is desired and necessary. Leu and Chang[64] summarized the existing segmentation methods as comprising three categories: thresholding, region oriented, and boundary detection and their detailed classification is reproduced in Fig. 7. In this current work, the boundary detection is re-divided into two groups, namely gradient detection and Laplacian detection, which is in accordance with the different principles of edge detection.[62]

The algorithms of boundary detection have been extensively adopted in the field of rock mass photogrammetry.[32,65] Hadjigeorgiou et al.[66] selected six representative algorithms from the boundary detection group and conducted an evaluation of their performance for constructing discontinuity traces. They concluded that these algorithms are incapable of the automatic extraction of discontinuity traces and attributed it to three reasons: (1) recognition of discontinuity traces is generally incomplete; (2) a manual search for the optimal threshold value for each image blocks the automation; and (3) binary images derived from segmentation are commonly contaminated by a large number of error pixels, and therefore require subsequent processing to remove them. Many efforts have been devoted to addressing these three issues.

For the incompleteness, Lemy and Hadjigeorgiou[67] proposed a segment linking method based on direction examination and aided by a dilation operation; Reid and Harrison[61] suggest three criteria for segment linking to ensure suitability. However, the performance of the two methods depends on a manual adjustment of a series of parameters (including distance, direction angle, brightness, and filter size), which presents a significant obstacle to the automation of the image processing.

In terms of manual interference, Lemy and Hadjigeorgiou[67] and Mohebbi et al.[68] fixed the threshold at a low value in order to strike a balance between automation and recognition performance. This approach apparently sacrifices the recognition performance, as the low threshold value will inevitably result in a large quantity of erroneous responses. Kuang and Zhang[69] introduced an adaptive Canny operator to realize recognition automation, however, this operator cannot effectively reduce the influence of noise. Zhang et al.[20] proposed a hybrid algorithm combining global and local thresholding. Essentially, this algorithm did not eliminate manual interference, because the selection of local region size was still non-automatic. Post et al.,[70] Deb et al.,[60] and Mohebbi et al.[68] suggested using the Hough transform as an alternative approach to extract discontinuity traces from any given binary images. The Hough transform recognizes discontinuities by solely finding pixels lying on straight lines. Therefore, without an effective procedure to remove noises, its performance was not reliable and robust.

As for error pixels removal, Lemy and Hadjigeorgiou[67] used artificial neural networks to separate segments representing discontinuity traces from other noise. Guo et al.[71] introduced a machine learning algorithm into the classification of discontinuity traces and noise while Kuang and Zhang[69] applied thresholding to the geometrical parameters of segments in order to filter noise. Artificial neural network and other supervised (or semi-supervised) machine learning techniques require training examples prepared by manual workers. Furthermore, the poor performance caused by either overfitting or underfitting is still challenging to avoid.

The effectiveness of these three methods is highly dependent on differentiating between the geometrical expression of discontinuity traces and noise. However the difference can be small and highly difficult to detect because of the rough edges on the rock face and, possibly, poor imaging conditions. These factors restrict the wide application of these methods.

In the following section, a novel approach for the automatic extraction of discontinuity areas is proposed based on the region growing approach. Compared with the reported methods above, this method features high noise resistance and full automation.

3.3.1. Region growing

Examining Fig. 6a, it can be observed that the pixels containing rough edges and dents were mapped at intensity levels similar to the discontinuity areas. These non-discontinuity pixels are noise that needs to be removed for better recognition of the discontinuities. In this work, a trial test on the effectiveness of boundary detection algorithms as described in Fig. 7 was initially conducted. The segmentation of Fig. 6a presented a result which was found to be similar to that of Hadjigeorgiou et al.,[66] and the result can be summarized as the incompleteness of recognition and a large number of erroneous responses. The outcomes of Canny operator[72] were taken as an example to illustrate the misleading issues. Using the Canny operator requires the manual adjustment of two parameters that represent high and low thresholds. Fig. 8 exhibits the outcomes of using the Canny operator with varying values of thresholds. Low thresholds produced images with much noise. Increasing the thresholds did not lead to an obvious suppression of noise, but it gradually erased the discontinuity traces.

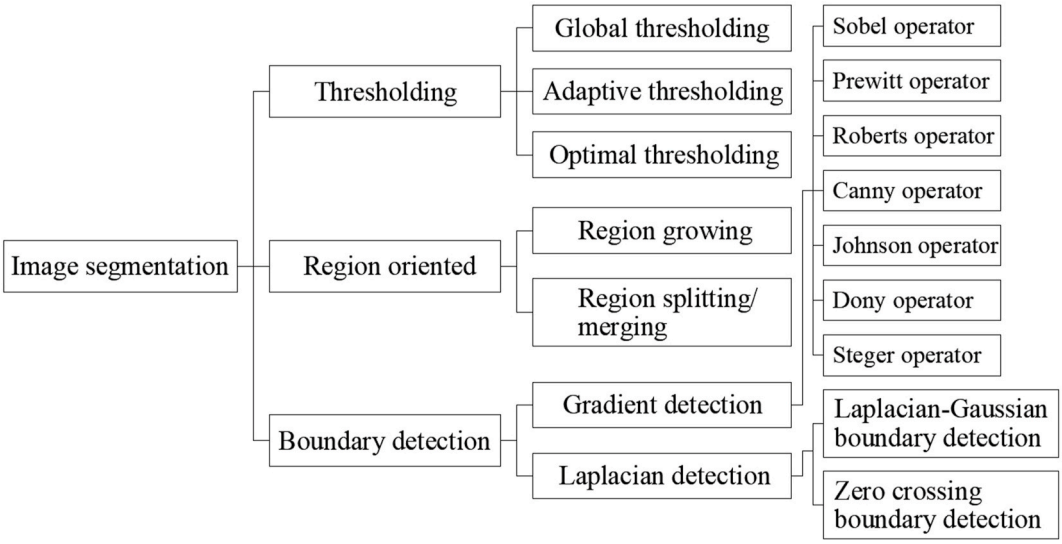

Fig. 7. Classification of image segmentation methods, after Leu and Chang.[64]

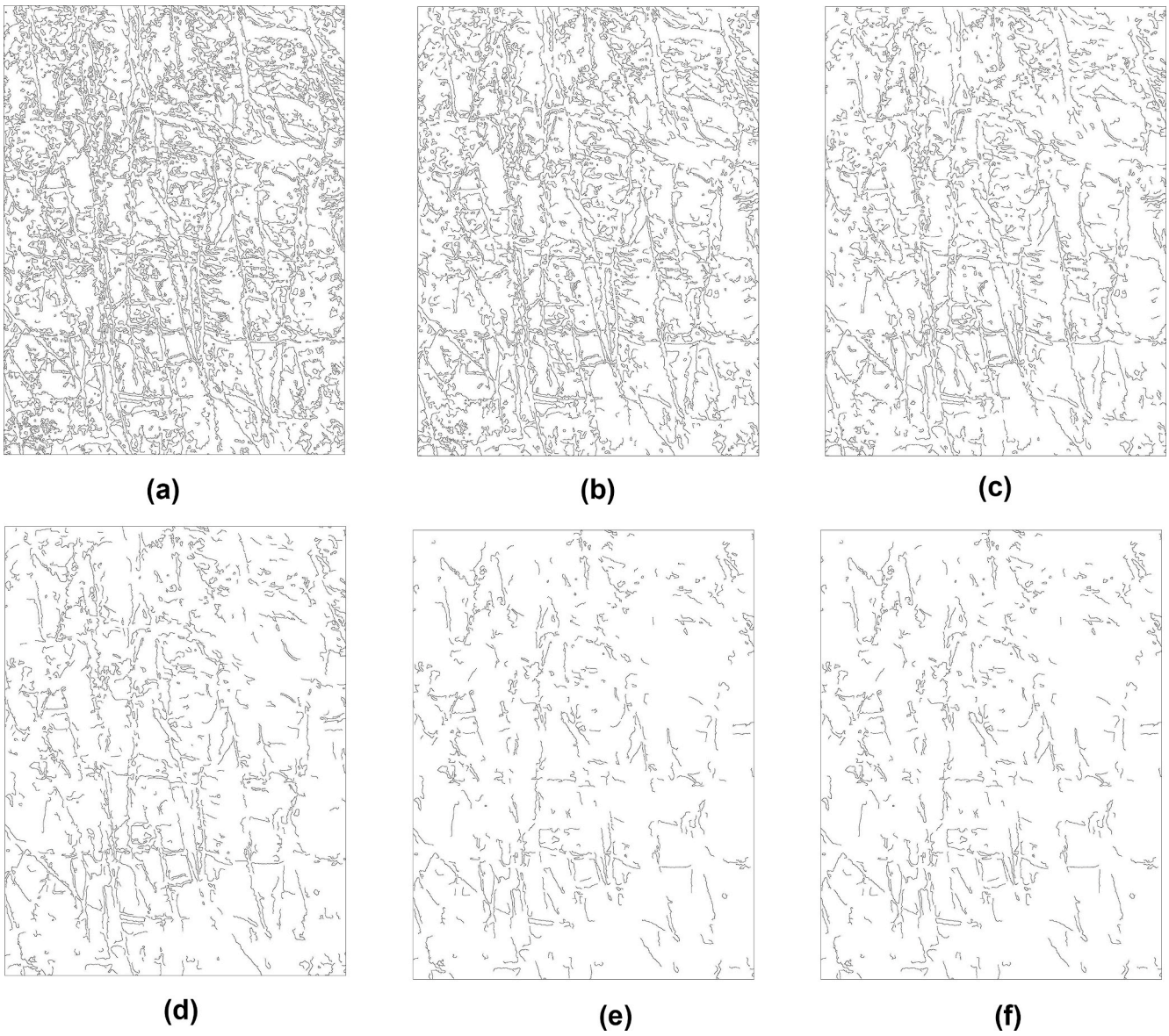

Fig. 8. Outcomes of using the Canny operator with high and low thresholds of: (**a**) 0.3 and 0.12, (**b**) 0.4 and 0.16, (**c**) 0.5 and 0.2, (**d**) 0.6 and 0.24, (e) 0.7 and 0.28, (f) 0.8 and 0.32.

After realizing the weakness of these boundary detection algorithms, we re-examined Fig. 6a and found two distinctions between discontinuities and noise. First, it was found that the pixels of discontinuity areas are closer to the lowest level (zero) even though the pixels of discontinuity areas and noise both had low intensity levels. Second, the discontinuity areas commonly intersect or link with noise areas, but they rarely merged, which indicates a fair degree of geometric independence.

Given that there is no clear boundary of intensity level between discontinuity areas and noise, the algorithms of the thresholding groups (see Fig. 7) were incapable of denoising. In some cases, the implementation of local thresholding would induce an adverse result—amplification of noise.[73] Recognizing this, we suggest adopting region growing to directly locate discontinuity areas, thereby separating them from the image noise. Region growing is an approach that combines pixels or subregions into larger regions based on predefined criteria. This process uses a set of "seed" points to mark the regions of interest, and then grows each seed by adding neighboring pixels that have properties close to the seed.[62]

For the selection of seeds for Fig. 6a, as discussed before, the pixels of discontinuity areas were found to have intensity level of approximately zero. Thus, the pixels with the five lowest intensity levels (0–4) were chosen as the seeds. There are two criteria for growing. The first is that the pixel should be 8-connected[62] to at least one pixel in a region in order to be included in it. If a pixel is found to be connected to more than one region, the regions should be merged. The second is that the intensity level of any pixel should be strictly less than 50. This number is a termination point for the region growing and was determined from a visual examination of Fig. 6a.

As mentioned in Section 3.2, the recognition of discontinuities relies on a detection of ravine structures, which are formed by low-level pixels. An appropriate threshold of intensity is necessary for the determination of the ravine boundary. Fig. 9a shows the binary image produced by region growing. Noise still exists, but it is significantly reduced compared to the boundary detection method shown in Fig. 8.

3.3.2. *Hough transform*

In Fig. 9a, most discontinuity areas are present as a combination of several segments. The break points and width variation are consistent with the irregularity of natural discontinuities. In addition, there are still a few small spots (or noise) scattered over Fig. 9a, which were caused by

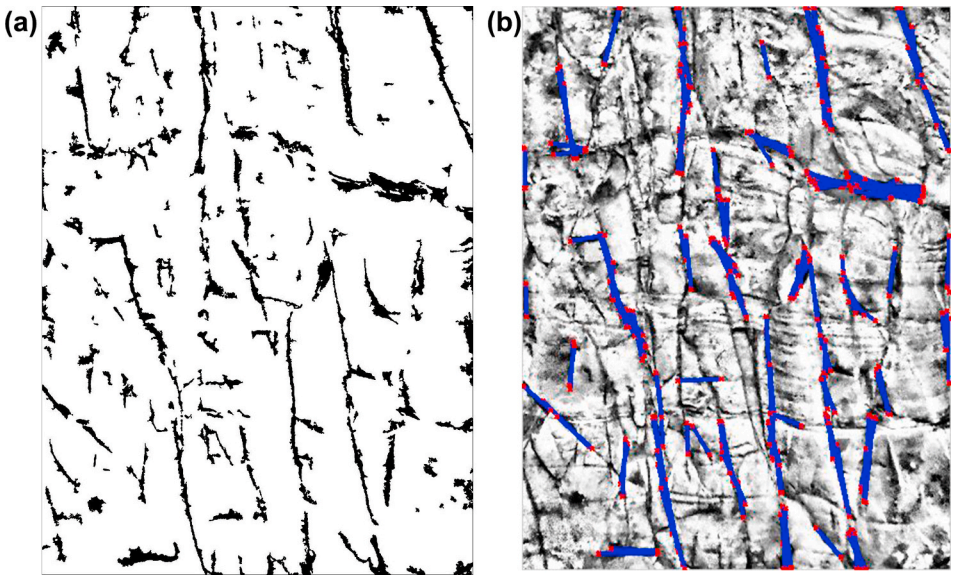

Fig. 9. (**a**) Binary image produced by region growing and (**b**) comparison between lines detected by Hough transform and the greyscale image.

seeds lying on non-discontinuity areas. A method is thus required to link segments and remove noise. The Hough transform is used to recognize discontinuities by finding pixels lying on straight lines, therefore, its performance can be dramatically reduced in a strong noise environment (*e.g.* images in Fig. 8). The region growing process effectively suppresses noise and thus provides a favorable condition for the implementation of the Hough transform.

The Hough transform describes a line, which is defined by two points (x_i, y_i) and (x_j, y_j), in the image plane (Fig. 10a) by using the following parametric equation:

$$x \cos\theta + y \sin\theta = \rho \tag{19}$$

where ρ denotes the length of a normal from the origin to the line, ranging from $-D_\rho$ to D_ρ. D_ρ is the diagonal length of the image under consideration. θ is the orientation of the normal with respect to the x-axis, ranging from -90° to 90°, and the clockwise direction is positive. Fig. 10b shows the parametric plane $\theta\rho$ of the Hough transform. Every sinusoidal curve represents a set of lines intersecting at a given point (x_n, y_n) on the image plane. On the parametric plane, the intersection point (θ', ρ') corresponds to the line that contains points (x_i, y_i) and (x_j, y_j) on the image plane.

The subdivision of the parametric plane into accumulator cells can significantly facilitate image recognition, which is an advantage of the Hough transform. Each (x, y) point can be transformed into a discretized curve, and the accumulator cells transited by the curve are incremented. After the accumulation of all points in the image plane, the peak value of the accumulator array indicates that a corresponding straight line exists. The size ($\Delta\rho$ and $\Delta\theta$) of the accumulator cells determines the accuracy of the Hough transform and here $\Delta\rho$ and $\Delta\theta$ are set as 1 pixel and 0.1°, respectively. A comparison between lines detected by the Hough transform and the greyscale image is shown in Fig. 9b. The lines are shown as blue segments with red endpoints. It can be seen that the discontinuity areas are separated from the rock face and the completeness is properly preserved—this is a desirable outcome.

3.3.3. *Unification of line aggregates*

The line aggregates derived from the Hough transform cannot be used directly for the characterization of discontinuities. An algorithm proposed by Edelsbrunner et al.[74] was employed to unify each aggregate as an area with a single boundary. A line aggregate can be transformed into a set of pixels (an 8-connected region), by adjusting the parameter α in the Edelsbrunner et al. formulation. The algorithm constructs a series of straight-line graphs to connect the extreme points of the pixel set. These graphs are the α-shape of the pixel set. For an α tending to infinity, an α-shape becomes the convex hull of the pixel set. When α tends to zero, an α-shape shrinks into separate pixels. The algorithm identifies the minimum value of α required to produce a straight-line graph enclosing the pixel set as a single area. The application of Edelsbrunner's algorithm to each line aggregate of Fig. 9b results in the final shape of the discontinuity areas.

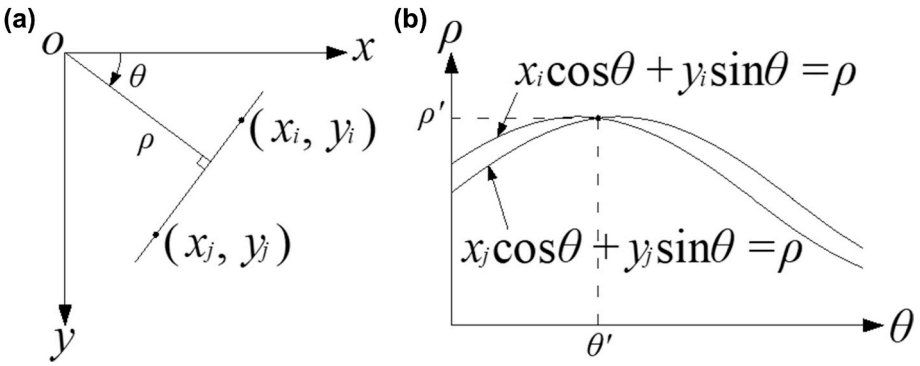

Fig. 10. Schematic diagram of the Hough transform: (**a**) image plane and (**b**) parametric plane.

3.4. Discontinuity characterization

3.4.1. Area thinning and skeleton linking

Two geometrical parameters for discontinuity characterization are length and orientation. Measurements of the two parameters should be conducted on a proper representation of discontinuity areas, *i.e.* a discontinuity trace. The discontinuity trace refers to a minimally connected line located at the middle. As the first step of discontinuity trace extraction, a thinning algorithm by Lam et al.[75] was adopted to obtain area skeletons. Subsequently, an algorithm is proposed to link skeletons automatically. This is based on the observation that several discontinuities were mistakenly recognized as several disconnected skeletons. Two examined skeletons are linked at the closest pair of pixels, if the following two conditions are verified: (1) if in the binary image (Fig. 9a), two pixel sets, whose space coordinates were the same as those of the two skeletons respectively, are 8-connected; (2) if the angle between the two skeletons does not exceed 45° with the direction of skeleton being determined by measuring the angle between the horizontal axis and the major axis of the ellipse that has the same second-moments as the skeleton.

The processed image after the linking operation is shown in Fig. 11a. Obviously, there were plenty of "spurs" on each skeleton, which hinders the measurements of discontinuity length and orientation. Conventional methods of spur removal deletes every endpoint pixel of the skeleton for predetermined times.[73] This procedure eliminates pixels in the discontinuity trace and needs manual intervention for determining the times to delete. An algorithm involving three steps is proposed here: (1) specify extrema points for each skeleton in eight directions (top-left top-right right-top right-bottom bottom-right bottom-left left-bottom left-top); (2) find the farthest pair of extrema points and mark them as the endpoints of the discontinuity trace; (3) substitute the endpoint pair into a path-finding algorithm by Eddins (see webpage: https://blogs.mathworks.com/steve/2011/12/13/exploring-shortest-paths-part-5/) to extract the discontinuity trace. Thirty three discontinuity traces were obtained by adopting this algorithm for processing our image, and they are shown in Fig. 11b. As mentioned above, the resolution of the rock face image is 1268 × 1671 pixels, the areal joint count (J_a) is calculated to be 1199 joint/m^2 by substituting the resolution into Equations (7) and (8). By assuming the rock is homogeneous, the volumetric joint count (J_v) of Equation (2) can be calculated by the following equation:

$$J_v = (J_a)^{\frac{3}{2}} \tag{20}$$

The result is 41517 joint/m^3. This excessive value was due to the small size of the laboratory sample. The length of recognized discontinuities ranges from 11.1 to 72.7 mm (as listed in the Appendix). When the object imaged is a rock face of roadway driving (commonly 4–5 m in width), the length of recognized discontinuities is likely to be dramatically increased, the value of J_v would decrease correspondingly. The field application of this algorithm is detailed in Section 4.

The length of the discontinuity (in terms of pixel distance) was measured by calculating the quasi-Euclidean length of the discontinuity trace. The real length was derived by substituting pixel length into Equation (9). The orientation of the discontinuity was determined by measuring the angle between the horizontal axis and the major axis of the ellipse that has the same second-moments as the discontinuity trace. The range of orientation is from −90° to 90°. A summary of rock sample discontinuity data is given in the Appendix.

3.4.2. Measurement of separation width and roughness

A commonly adopted algorithm for the measurement of separation width is a best-fit rectangle,[76] and it is suitable for an object with a regular shape. But a natural discontinuity is characterized by shape variation and cutting points. Therefore, we developed an algorithm to measure the separation width by sampling transections of the discontinuity area in the binary image (Fig. 9a). There are two types of sampling methods dealing with two ranges of discontinuity orientation (θ_m), respectively. For $-90° < \theta_m < -60°$ and $60° < \theta_m \leq 90°$, the sampling lines are aligned perpendicular to the line (L_a) that is determined by the upper endpoint of the discontinuity trace and θ_m. They are equally spaced at a distance of $D_i/sin\,|\theta_m|$, here, D_i denotes the sampling interval (in terms of pixel distance). The lengths of intersections between the discontinuity area and sampling lines make up the sample set, and the median value of the set is considered to be the final value for separation width. For $-60° \leq \theta_m \leq 60°$, the sampling lines are aligned perpendicular to the line (L_a) that is determined by the left endpoint of

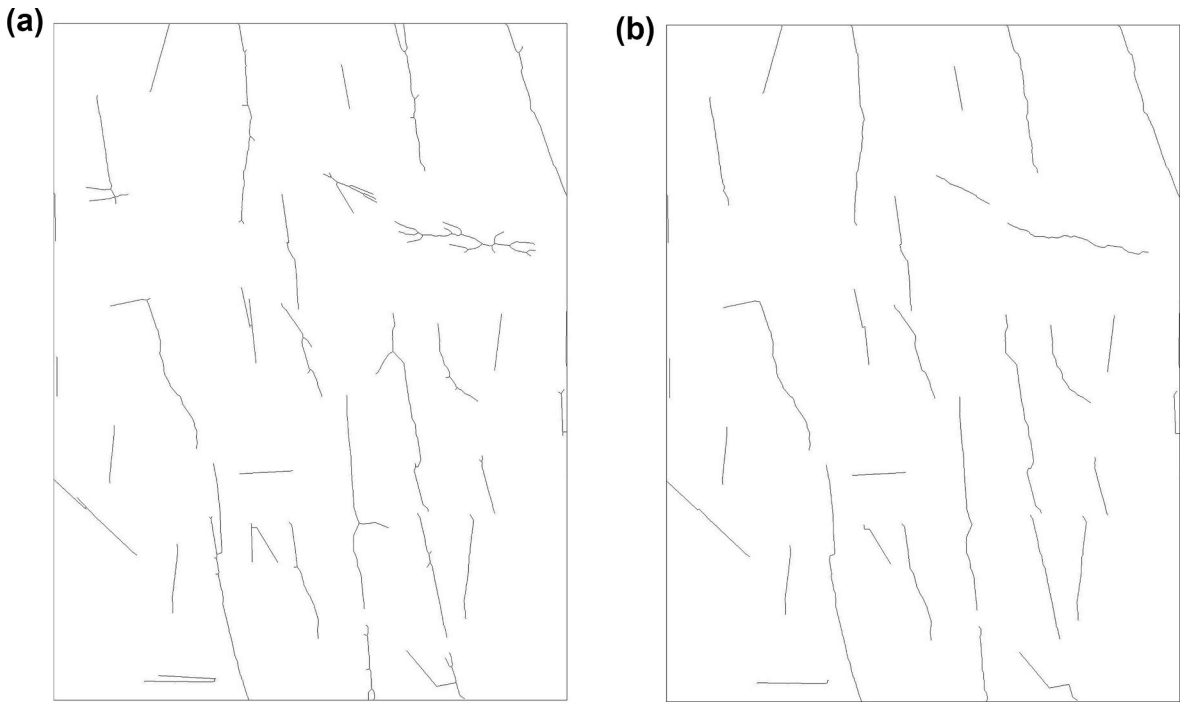

Fig. 11. (**a**) Processed image of linking operation and (**b**) outcome of spurs removal.

discontinuity trace and θ_m. They are equally spaced at a distance of $D_i/cos\,|\theta_m|$. The final value of separation width is the median value of the sample set and the real separation width can then be derived by substituting the pixel distance into Equation (10). The separation width of discontinuities is listed in the Appendix.

The roughness of a discontinuity was calculated by using Equation (4) and the data for *JRC* calculation was acquired through measuring the deviation of a discontinuity trace from the reference line determined by an endpoint of the discontinuity trace and θ_m. The sampling method was the same as for the separation width measurement. For a *JRC* value larger than 20, it should be specified as 20. The derived data are presented in the Appendix.

3.4.3. Comparison with the hand-drawn trace map

A discontinuity trace map of the virgin image was drawn using a pen and a sheet of transparent tracing paper. It was then digitized and is shown in Fig. 12a. In order to present a complete comparison, the traces generated by the automatic methodology and the virgin image are included in Fig. 12b and c, respectively. Obviously, the two trace maps are broadly comparable with a moderate difference in the shape of the curves. The length of each trace in the hand-drawn map was directly measured using a measuring tape. The *JRC* calculation was performed on the digitized representation (*i.e.* Fig. 12a) by measuring the deviation of the discontinuity trace from the reference line determined by an endpoint of the trace and the discontinuity orientation. The sampling interval was set as 2 mm. The resulting data was substituted into Equation (4). A comparison of the measurements using different trace maps is given in Fig. 13. It can be observed from Fig. 13a that the length values calculated using the machine-recognized trace map are close to those using the hand-drawn map. This conclusion is also strong evidence of the validity of separation width measurements in Section 3.4.2 because the basic principles behind the separation width and length calculations are the same. They both derive values from the transformation of pixel distance, *i.e.* Equations (9) and (10). Fig. 13b indicates that the *JRC* values calculated from the machine-recognized trace map roughly agree with those calculated from the hand-drawn map. The median of the former *JRC* values is 3.5, and the latter median is 3.2. This agreement demonstrates that the effect of several deviations (exhibited in Fig. 13b) is limited, as the median is the representative value using for *GSI* calculation in Section 4.

4. Application of the proposed algorithm to mine case studies

4.1. Mine case study - I

A rock face photo (with a resolution of 3340 × 2500 pixels and shown in Fig. 14a) was taken at an excavation face of an underground coal mine located in Changwu County, Shaanxi Province, China. The roadway was designed to be positioned at the middle of the No. 4 coal seam. A geologic column of the roof and floor of the No. 4 coal seam is illustrated in Fig. 14b. Due to the influence of a fault, the roadway was driven into the roof and reached to the junction of fine sandstone and coarse sandstone, where the photo was taken. The camera lens was placed normal to the rock face, and the distance between lens and rock face was measured as 2.08 m using a laser range meter. The real area of rock face shown in Fig. 14a is calculated to be 4.65 m^2 by substituting the working distance and resolution into Equations (7) and (8). Since the diffuse lamp mentioned in Section 3.1.1 is not intrinsically safe for underground application, a cap lamp and a wall-mounted lamp, which are both direct lighting sources, were utilized as the lighting. The original GSI chart[41,42] was applied to the excavation face, and the rating was found to be in the range from 50 to 56.

The rock face in Fig. 14a was covered in scratches from the cutting head, which led to poor contrast between discontinuity and the intact rock. Fig. 14a also shows 10 discontinuity traces (in yellow) produced by the algorithm described in Section 3. Despite the undesired lighting source, traces were correctly recognized at the location of discontinuities. Moreover, both linear and curved components of discontinuity traces were properly preserved. This performance demonstrates that the algorithm is capable of rejecting the impact of mechanical scratches and thus possesses a strong adaptability. The areal and volumetric joint counts were calculated to be 2.15 joint/m^2 and 3.15 joint/m^3, respectively. The median values of separation width and *JRC* are 11.95 mm and 10.3, respectively. They were chosen as the representative values and substituted into Equations (2) and (5). The resulting value of the GSI rating is 51. It agreed well with the rating obtained by field survey, which demonstrates that the proposed algorithm can be applied in the engineering environment of roadway driving.

4.2. Mine case study - II

The photo in Fig. 15a shows a roof seam outcrop located at Yuwu Town, Tunliu County, Shanxi Province, China. The rock mass appears to be highly fractured and is split by an approximately 45° fault. Similarly

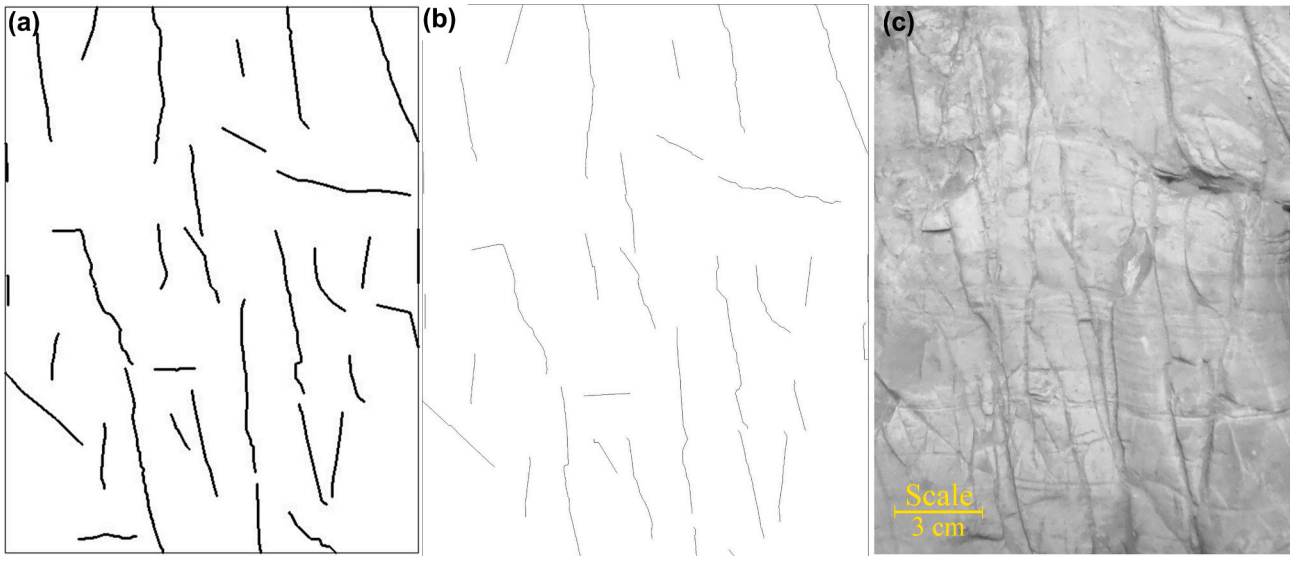

Fig. 12. Comparison of discontinuity trace maps: (**a**) hand-drawn trace map, (**b**) traces generated by the automatic methodology, and (**c**) virgin image.

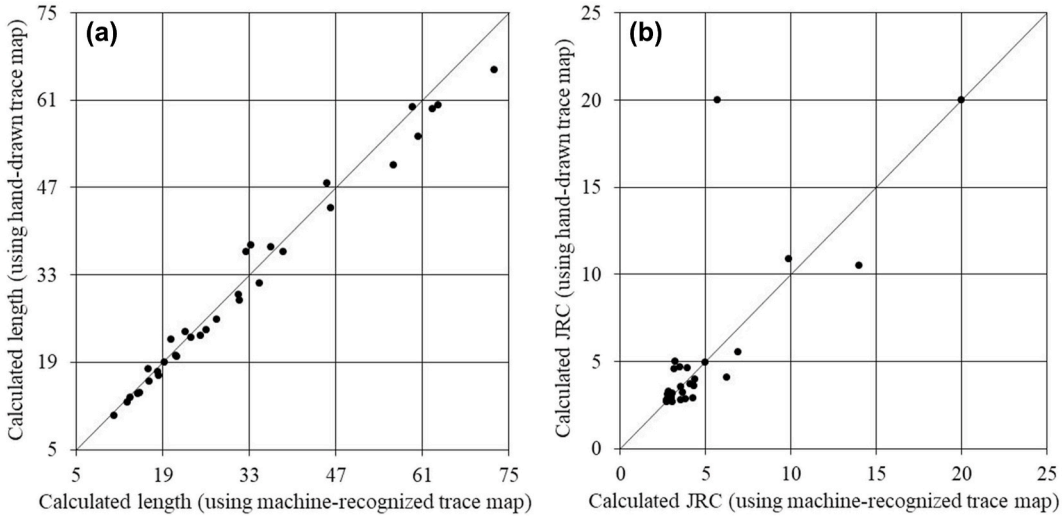

Fig. 13. Comparison of the (**a**) calculated length and (**b**) calculated JRC using different trace maps.

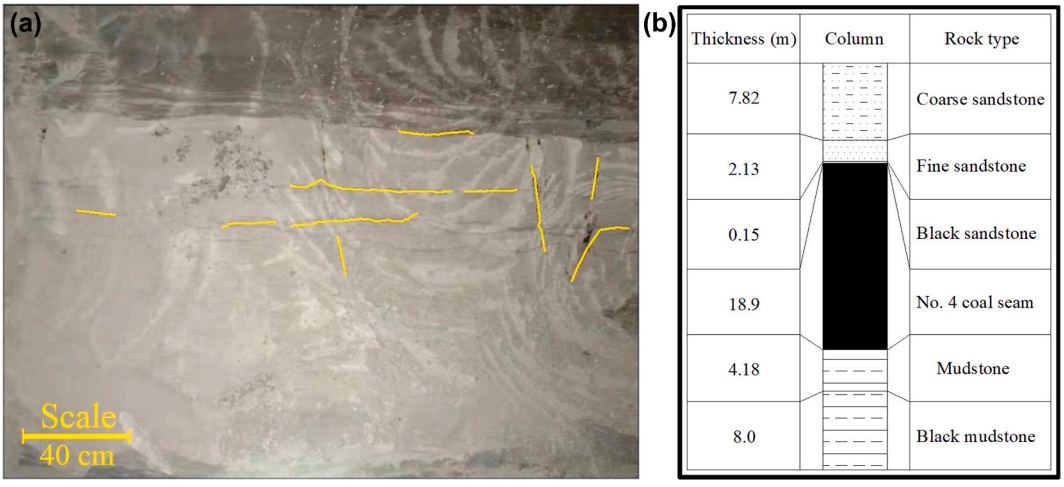

Fig. 14. (**a**) Photograph of a rock face in roadway excavation and (**b**) geologic column of the roof and floor of No. 4 coal seam.

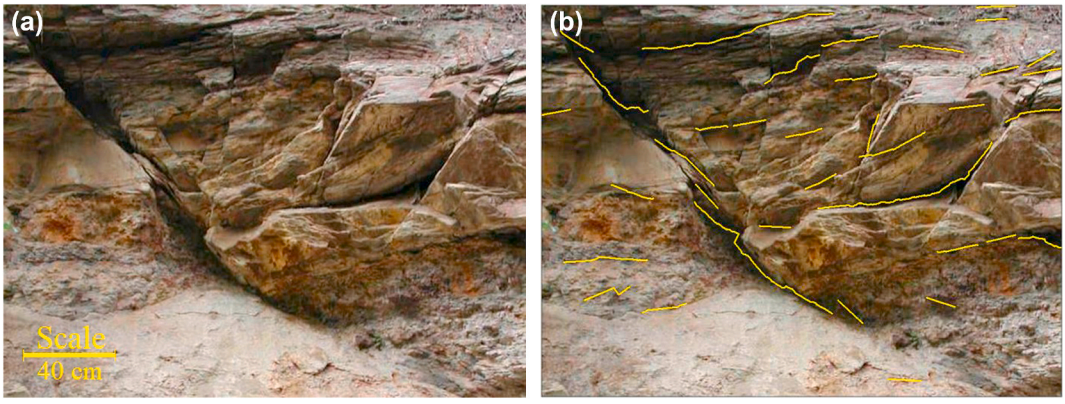

Fig. 15. (**a**) Photo of a roof seam outcrop and (**b**) corresponding discontinuity traces.

to case I, the camera lens was placed normal to the rock face, and the distance between lens and rock face was measured as 1.64 m using a laser range meter. The image acquisition was conducted under natural lighting. The unevenness of the outcrop leads to a shadow effect, *i.e.,* a gradual increase in brightness from the top left corner to the bottom right corner. The resolution of Fig. 15a is 4000 × 3000 pixels, and the real area is calculated to be 4.16 m^2 by using Equations (7) and (8). The original GSI chart[41,42] was applied to the outcrop, and the rating was estimated to be in the range of 20 ~ 26.

An obvious difference between images of Figs. 15a and 14a is that the

exposure is strewn with numerous small rock fragments. As shown in the work conducted by Hadjigeorgiou et al.,[66] the adverse effect of these fragments on the discontinuity recognition would be amplified by shadows, which leads to many erroneous responses in common edge detection algorithms. Thirty six discontinuity traces in Fig. 15b were produced by our proposed algorithm. Obviously, it precisely located the discontinuities while capturing their geometrical features. The areal and volumetric joint counts were calculated as 8.66 joint/m^2 and 25.50 joint/m^3, respectively. The representative values of separation width and *JRC* were chosen as their median values, *i.e.* 23.8 mm and 7.6, respectively. The resulting value of the GSI rating is 24—which agreed well with the field survey results. The consistency with field results verifies the adaptability and effectiveness of the proposed algorithm.

5. Summary and conclusions

A rapid and robust acquisition method for rock mass engineering properties is a persistent concern for underground engineering practitioners who must use those properties to design safe subsurface rock structures. We provide a robust system for the automatic determination of the GSI rating based on images of in-situ fractured rock masses. A series of novel algorithms were proposed to extract data essential for determining the GSI rating from the fractured rock mass images. The effectiveness and accuracy of this automatic image-based GSI rating system are validated by both experimental and field studies. A few main conclusions can be drawn as follows:

(1) The original GSI rating is calculated by inputting qualitative parameters, which renders the system somewhat subjective and hard to apply to digital image analysis. A quantified GSI system was developed by using *SR* and *JCDI* to represent the blockiness and discontinuity surface condition of the rock mass. The system provides a quantitative numerical basis for the automatic calculation of the GSI rating.
(2) Local histogram equalization and self-adaptive gamma correction were introduced into the preprocessing of the rock face images. Compared to conventional histogram equalization, local histogram equalization can effectively restrain uneven distribution of brightness. Self-adaptive gamma correction can automatically enlarge the difference between discontinuity areas and the intact rock face based on the image properties.
(3) A novel algorithm combining region growing and the Hough transform was proposed for the automatic extraction of discontinuity areas. Laboratory and field tests demonstrate that the algorithm has the advantage of better noise suppression compared to existing methods and can yield reasonable results for images taken in poor photographing conditions.
(4) Discontinuities were characterized by a novel algorithm comprising area thinning, skeleton linking, spurs removal, and sampling. Using this algorithm, four parameters of the discontinuity can be quantified: length, orientation, separation width, and *JRC* value.

The system developed in this study is a flexible and adaptable technique that can provide operators with timely information on rock mass engineering properties. It avoids the biases associated with visual observation and significantly reduces the time required to be spent under unsafe conditions. Most importantly, it raises the possibility of the creation of a permanent and huge database of ground engineering properties.

Declaration of competing interest

The authors declare that they have no known competing financial interests or personal relationships that could have appeared to influence the work reported in this paper.

Acknowledgements

This work was partially supported by the National Institute of Occupational Safety and Health (NIOSH) [grant number NIOSH-200-2016-90385]; the National Natural Science Foundation of China [grant numbers 52004204, 51574224], and the National Key Research and Development Program [grant number 2016YFC0600901].

Appendix A. Summary of the geometrical data of discontinuities

No.	Length (pixel distance)	Length (mm)	Orientation (°)	Separation width (pixel distance)	Separation width (mm)	JRC value
1	120.6	13.7	−89.1	6.0	0.7	3.0
2	284.8	32.5	−42.4	4.2	0.5	2.8
3	97.4	11.1	−90.0	11.5	1.3	2.7
4	292.3	33.3	−80.5	10.2	1.2	3.0
5	147.8	16.8	84.7	13.0	1.5	2.8
6	520.8	59.4	−65.3	14.8	1.7	20.0
7	185.4	21.1	−0.1	21.5	2.4	3.5
8	186.5	21.3	74.3	15.8	1.8	2.8
9	177.9	20.3	84.8	8.0	0.9	3.0
10	637.6	72.7	−83.0	12.0	1.4	4.3
11	529.3	60.3	90.0	13.5	1.5	3.9
12	133.9	15.3	3.1	10.0	1.1	2.8
13	206.6	23.5	−78.2	11.2	1.3	3.2
14	130.4	14.9	−55.7	25.2	2.9	3.8
15	275.6	31.4	−68.4	17.9	2.0	5.0
16	304.5	34.7	−80.8	12.2	1.4	3.7
17	320.1	36.5	−74.1	11.4	1.3	4.3
18	160.8	18.3	−27.8	19.3	2.2	3.1
19	116.3	13.3	−79.5	26.5	3.0	2.7
20	558.3	63.6	−85.5	10.0	1.1	4.1
21	198.9	22.7	−84.7	16.0	1.8	3.6
22	549.0	62.6	−80.3	10.2	1.2	6.9
23	404.5	46.1	−80.0	20.4	2.3	4.4
24	399.0	45.5	−10.8	39.6	4.5	6.2
25	220.4	25.1	−35.1	34.4	3.9	14.0
26	337.1	38.4	−77.2	7.3	0.8	3.0

(*continued on next page*)

(*continued*)

No.	Length (pixel distance)	Length (mm)	Orientation (°)	Separation width (pixel distance)	Separation width (mm)	JRC value
27	243.4	27.7	−64.6	7.8	0.9	9.9
28	274.0	31.2	84.7	16.1	1.8	3.0
29	158.6	18.1	−76.3	13.6	1.5	3.2
30	146.0	16.6	83.1	23.6	2.7	2.7
31	494.6	56.4	−71.3	13.9	1.6	3.5
32	228.0	26.0	−85.1	16.5	1.9	5.7
33	169.5	19.3	89.3	22.0	2.5	2.8

References

1 Karra VK. Analysis of non-fatal and fatal injury rates for mine operator and contractor employees and the influence of work location. *J Saf Res*. 2005;36:413–421.
2 Chen H, Qi H, Long R, Zhang M. Research on 10-year tendency of China coal mine accidents and the characteristics of human factors. *Saf Sci*. 2012;50:745–750.
3 Shen B. Coal mine roadway stability in soft rock: a case study. *Rock Mech Rock Eng*. 2014;47:2225–2238.
4 Shi Y, Yang J, Wang S. Sub-horizontal reinforcement of weathered granite before tunneling beneath a spillway. *Int J Rock Mech Min Sci*. 2014;72:283–293.
5 Lu W, Wang Q, , et alJiang Z. Comparative study on bearing mechanism and design parameters of confined concrete arch joints in deep soft rock roadway. *Int. J. Coal Sci. Tech.* 2019;6:493–504.
6 Zuo J, Wang J, Jiang Y. Macro/meso failure behavior of surrounding rock in deep roadway and its control technology. *Int. J. Coal Sci. Tech.* 2019;6:301–319.
7 Bieniawski ZT. Engineering classification of jointed rock masses. *Civ. Eng. S. Afr.* 1973;15:335–344.
8 Barton N, Lien R, Lunde J. Engineering classification of rock masses for the design of tunnel support. *Rock Mech*. 1974;6:189–236.
9 Hoek E. Strength of rock and rock masses. *ISRM News J*. 1974;2:4–16.
10 Hoek E, Brown ET. Practical estimates of rock mass strength. *Int J Rock Mech Min Sci*. 1997;34:1165–1186.
11 Molinda GM, Mark C. The Coal Mine Roof Rating (CMRR) - a practical rock mass classification for coal mines. In: Peng SS, ed. *12th Conference on Ground Control in Mining*. West Virginia: Morgantown; 1993:92–103.
12 Zhang L. Estimating the strength of jointed rock masses. *Rock Mech Rock Eng*. 2010;43(4):391–402.
13 Zhang L, Einstein HH. Estimating the mean trace length of rock discontinuities. *Rock Mech. Rock Eng. 1998*. 1998;31:217–235.
14 Sturzenegger M, Stead D. Close-range terrestrial digital photogrammetry and terrestrial laser scanning for discontinuity characterization on rock cuts. *Eng. Geol. 2009*. 2009;106:163–182.
15 Ferrero AM, Forlani G, Roncella R, Voyat HI. Advanced geostructural survey methods applied to rock mass characterization. *Rock Mech Rock Eng*. 2009;42:631–665.
16 Sturzenegger M, Stead D, Elmo D. Terrestrial remote sensing-based estimation of mean trace length, trace intensity and block size/shape. *Eng Geol*. 2011;119:96–111.
17 Riquelme AJ, Abellán A, Tomás R. Discontinuity spacing analysis in rock masses using 3D point clouds. *Eng Geol*. 2015;195:185–195.
18 Zhu H, Wu W, Chen J, Ma G, Liu X, Zhang X. Integration of three dimensional discontinuous deformation analysis (DDA) with binocular photogrammetry for stability analysis of tunnels in blocky rockmass. *Tunn Undergr Space Technol*. 2016;51:30–40.
19 Assali P, Grussenmeyer P, Villemin T, Pollet N, Viguier F. Solid images for geostructural mapping and key block modeling of rock discontinuities. *Comput Geosci*. 2016;89:21–31.
20 Zhang P, Zhao Q, Tannant DD, Ji T, Zhu H. 3D mapping of discontinuity traces using fusion of point cloud and image data. *Bull Eng Geol Environ*. 2018;78:2789–2801.
21 Umili G, Ferrero A, Einstein HH. A new method for automatic discontinuity traces sampling on rock mass 3D model. *Comput Geosci*. 2013;51:182–192.
22 Li X, Chen J, Zhu H. A new method for automated discontinuity trace mapping on rock mass 3D surface model. *Comput Geosci*. 2016;89:118–131.
23 Wang X, Zou L, Shen X, Ren Y, Qin Y. A region-growing approach for automatic outcrop fracture extraction from a three-dimensional point cloud. *Comput Geosci*. 2017;99:100–106.
24 Lato M, Diederichs MS, Hutchinson DJ, Harrap R. Optimization of LiDAR scanning and processing for automated structural evaluation of discontinuities in rockmasses. *Int J Rock Mech Min Sci*. 2009;1:194–199.
25 Gigli G, Casagli N. Semi-automatic extraction of rock mass structural data from high resolution LIDAR point clouds. *Int J Rock Mech Min Sci*. 2011;48:187–198.
26 García-Sellés D, Falivene O, Arbués P, Gratacos O, Tavani S, Munoz JA. Supervised identification and reconstruction of near-planar geological surfaces from terrestrial laser scanning. *Comput Geosci*. 2011;37:1584–1594.
27 Lato MJ, Vöge M. Automated mapping of rock discontinuities in 3D lidar and photogrammetry models. *Int J Rock Mech Min Sci*. 2012;54:150–158.
28 Vöge M, Lato MJ, Diederichs MS. Automated rockmass discontinuity mapping from 3-dimensional surface data. *Eng Geol*. 2013;164:155–162.
29 Slob S, Van Knapen B, Hack R, Turner K, Kemeny J. Method for automated discontinuity analysis of rock slopes with 3D laser scanning. In: *Proceedings of the Transportation Research Board 84th Annual Meeting*. Washington D.C.; January 2005:187–194.
30 Slob S, Hack H, Feng Q, Roshoff K, Turner AK. Fracture mapping using 3D laser scanning techniques. In: *Proceedings of the 11th Congress of International Society for Rock Mechanics*. January 2007:299–302. Lisbon, Portugal.
31 Olariu MI, Ferguson JF, Aiken CLV, Xu X. Outcrop fracture characterization using terrestrial laser scanners: deep-water jackfork sandstone at big rock quarry. *Arkansas. Geosphere*. 2008;4:247–259.
32 Otoo JN, Maerz NH, Duan Y, Li XL. LiDAR and optical imaging for 3D fracture orientations. In: *Proceedings of the 2011 NSF Engineering Research and Innovation Conference*. 2011. Atlanta, Georgia.
33 Assali P, Grussenmeyer P, Villemin T, Pollet N, Viguier F. Surveying and modeling of rock discontinuities by terrestrial laser scanning and photogrammetry: semi-automatic approaches for linear outcrop inspection. *J Struct Geol*. 2014;66:102–114.
34 Riquelme AJ, Abellán A, Tomás R, Jaboyedoff M. A new approach for semi-automatic rock mass joints recognition from 3D point clouds. *Comput Geosci*. 2014;68:38–52.
35 Riquelme A, Tomás R, Cano M, Pastor JL, Abellan A. Automatic mapping of discontinuity persistence on rock masses using 3D point clouds. *Rock Mech Rock Eng*. 2018;51:3005–3028.
36 Cacciari PP, Futai MM. Modeling a shallow rock tunnel using terrestrial laser scanning and discrete fracture networks. *Rock Mech Rock Eng*. 2017;50:1217–1242.
37 Long NQ, Buczek MM, , et alCuong CX. Accuracy assessment of mine walls' surface models derived from terrestrial laser scanning. *Int. J. Coal Sci. Tech.* 2018;5:328–338.
38 Huang JZ, Feng XT, Zhou YY, Yang CX. Stability analysis of deep-buried hard rock underground laboratories based on stereophotogrammetry and discontinuity identification. *Bull Eng Geol Environ*. 2019;78:5195–5217.
39 Fan L, Ma L, Yu Y, Wang S, Xu Y. Water-conserving mining influencing factors identification and weight determination in northwest China. *Int. J. Coal Sci. Tech.* 2019;6:95–101.
40 Smith JA. Analysis of the influence of groundwater and the stress regime on bolt behaviour in underground coal mines. *Int. J. Coal Sci. Tech.* 2019;6:286–300.
41 Hoek E. Putting numbers to geology–an engineer's viewpoint. *Q J Eng Geol Hydrogeol*. 1999;32:1–19.
42 Hoek E, Marinos P. Predicting tunnel squeezing problems in weak heterogeneous rock masses. *Tunnels Tunn Int*. 2000;32:45–51.
43 Sonmez H, Ulusay R. Modifications to the geological strength index (GSI) and their applicability to stability of slopes. *Int J Rock Mech Min Sci*. 1999;36:743–760.
44 Sonmez H, Ulusay R. A discussion on the Hoek-Brown failure criterion and suggested modifications to the criterion verified by slope stability case studies. *Yerbilimleri*. 2002;26:77–99.
45 Russo G. A new rational method for calculating the GSI. *Tunn Undergr Space Technol*. 2009;24:103–111.
46 Cai M, Kaiser PK, Uno H, Tasaka Y, Minami M. Estimation of rock mass deformation modulus and strength of jointed hard rock masses using the GSI system. *Int J Rock Mech Min Sci*. 2004;41:3–19.
47 Agliardi F, Sapigni M, Crosta GB. Rock mass characterization by high-resolution sonic and GSI borehole logging. *Rock Mech Rock Eng*. 2016;49:4303–4318.
48 Hoek E, Carter TG, Diederichs MS. Quantification of the geological strength index chart. In: *Proceedings of the 47th US Rock Mechanics/geomechanics Symposium*. January 2013. San Francisco, California.
49 Palmström A. Measurements of and correlations between block size and rock quality designation (RQD). *Tunn Undergr Space Technol*. 2005;20:362–377.
50 Palmström A. The volumetric joint count—a useful and simple measure of the degree of jointing. In: *Proceedings of the Fourth Congress International Association of Engineering Geology*. 1982:221–228. New Delhi.
51 ISRM. Suggested methods for the quantitative description of discontinuities in rock masses. *Int J Rock Mech Min Sci Geomech Abstr*. 1978;15:319–368.
52 Palmström A. Characterizing rock masses by the RMi for use in practical rock engineering, part 1: the development of the Rock Mass index (RMi). *Tunn Undergr Space Technol*. 1996;11:175–188.
53 Barton N, Choubey V. The shear strength of rock joints in theory and practice. *Rock Mech*. 1977;10:1–54.
54 Myers NO. Characteristics of surface roughness. *Wear*. 1962;5:182–189.
55 Bendat JS, Piersol AG. *Random Data Analysis and Measurement Procedures*. Toronto: Wiley Intersci; 1971.
56 Sayles RS, Thomas RR. The spatial representation of surface roughness by means of the structure functions, a practical alternative to correlation. *Wear*. 1977;42:263–276.
57 Tse R, Cruden DM. Estimating joint roughness coefficients. *Int J Rock Mech Min Sci Geomech Abstr*. 1979;16:303–307.

58 Maerz NH, Franklin JA, Bennett CP. Joint roughness measurement using shadow profilometry. *Int J Rock Mech Min Sci Geomech Abstr*. 1990;27:329–343.
59 Kazuya A, Hirofumi C. Efficient calibration of amateur digital camera and orientation for photogrammetric applications. In: *Proceedings of International Society for Photogrammetry and Remote Sensing*. Istanbul; 2004:149–152.
60 Deb D, Hariharan S, Rao UM, Ryu C. Automatic detection and analysis of discontinuity geometry of rock mass from digital images. *Comput Geosci*. 2008;34:115–126.
61 Reid TR, Harrison JP. A semi-automated methodology for discontinuity trace detection in digital images of rock mass exposures. *Int J Rock Mech Min Sci*. 2000;37:1073–1089.
62 Gonzales R, Woods R. *Digital Image Processing*. Addison-Wesley Publishing Co; 1992.
63 Huang S, Cheng F, Chiu Y. Efficient contrast enhancement using adaptive gamma correction with weighting distribution. *IEEE Trans Image Process*. 2013;22:1032–1041.
64 Leu S, Chang S. Digital image processing based approach for tunnel excavation faces. *Autom ConStruct*. 2005;14:750–765.
65 Azarafza M, Ghazifard A, Akgün H, Asghari-Kaljahi E. Development of a 2D and 3D computational algorithm for discontinuity structural geometry identification by artificial intelligence based on image processing techniques. *Bull Eng Geol Environ*. 2018;78:3371–3383.
66 Hadjigeorgiou J, Lemy F, Cote P, Maldague X. An evaluation of image analysis algorithms for constructing discontinuity trace maps. *Rock Mech Rock Eng*. 2003;36:163–179.
67 Lemy F, Hadjigeorgiou J. Discontinuity trace map construction using photographs of rock exposures. *Int J Rock Mech Min Sci*. 2003;40:903–917.
68 Mohebbi M, Yarahmadi Bafghi AR, Fatehi Marji M, Gholamnejad J. Rock mass structural data analysis using image processing techniques (case study: choghart iron ore mine northern slopes). *J. Min. Environ.* 2017;8:61–74.
69 Kuang J, Zhang Y. Automatic detection of rock mass discontinuity trace based on digital image processing. *Geotech. Eng. Tech.* 2017;31:5–13 (in Chinese).
70 Post RM, Kemeny JM, Murphy R. Image processing for automatic extraction of rock joint orientation data from digital images. In: *Proceedings of the 38th US Symposium on Rock Mechanics*. 2001:877–884. Washington, DC.
71 Guo L, Liao J, Dong K, et al. Automated detection of rock discontinuity trace based on digital image processing and svm. *J Sichuan Univ*. 2012;44:203–210 (in Chinese).
72 Canny J. A computational approach to edge detection. *IEEE Trans Pattern Anal Mach Intell*. 1986;6:679–698.
73 Li W, Liu G, Yao T. Improvement of methods for crack image processing and crack feature extraction of expansive soil. *Rock Soil Mech*. 2014;35:3619–3626 (in Chinese).
74 Edelsbrunner H, Kirkpatrick D, Seidel R. On the shape of a set of points in the plane. *IEEE Trans Inf Theor*. 1983;29:551–559.
75 Lam L, Lee SW, Suen CY. Thinning methodologies-a comprehensive survey. *IEEE Trans Pattern Anal Mach Intell*. 1992;14:879.
76 Wang W. Image analysis of particles by modified Ferret method—best-fit rectangle. *Powder Technol*. 2006;165:1–10.